Inorg. Chem. **2003**, *42*, 469–481

Inorganic Chemistry Article

Electronic Structure and Reactivity of High-Spin Iron–Alkyl- and –Pterinperoxo Complexes

Nicolai Lehnert,[†,‡] Kiyoshi Fujisawa,*[,§] and Edward I. Solomon*[,†]

Departments of Chemistry, Stanford University, Stanford, California 94305-5080, and University of Tsukuba, Tsukuba 305-8571, Japan

Received August 5, 2002

The spectroscopic properties and electronic structure of the four-coordinate high-spin $[Fe^{III}(L3)(OO^tBu)]^+$ complex (**1**; L3 = hydrotris(3-*tert*-butyl-5-isopropyl-1-pyrazolyl)borate; ^{t}Bu = *tert*-butyl) are investigated and compared to the six-coordinate high-spin $[Fe(6\text{-}Me_3TPA)(OH_x)(OO^tBu)]^{x+}$ system (TPA = tris(2-pyridylmethyl)amine, $x = 1$ or 2) studied earlier [Lehnert, N.; Ho, R. Y. N.; Que, L., Jr.; Solomon, E. I. *J. Am. Chem. Soc.* **2001**, *123*, 12802–12816]. Complex **1** is characterized by Raman features at 889 and 830 cm^{-1} which are assigned to the O–O stretch (mixed with the symmetric C–C stretch) and a band at 625 cm^{-1} that corresponds to ν(Fe–O). The UV–vis spectrum shows a charge-transfer (CT) transition at 510 nm from the alkylperoxo π^*_v (v = vertical to C–O–O plane) to a d orbital of Fe(III). A second CT is identified from MCD at 370 nm that is assigned to a transition from π^*_h (h = horizontal to C–O–O plane) to an Fe(III) d orbital. For the TPA complex the π^*_v CT is at 560 nm while the π^*_h CT is to higher energy than 250 nm. These spectroscopic differences between four- and six-coordinate Fe(III)–OOR complexes are interpreted on the basis of their different ligand fields. In addition, the electronic structure of Fe–OOPtn complexes with the biologically relevant pterinperoxo ligand are investigated. Substitution of the *tert*-butyl group in **1** by pterin leads to the corresponding Fe(III)–OOPtn species (**2**), which shows a stronger electron donation from the peroxide to Fe(III) than **1**. This is related to the lower ionization potential of pterin. Reduction of **2** by one electron leads to the Fe(II)–OOPtn complex (**3**), which is relevant as a model for potential intermediates in pterin-dependent hydroxylases. However, in the four-coordinate ligand field of **3**, the additional electron is located in a nonbonding d orbital of iron. Hence, the pterinperoxo ligand is not activated for heterolytic cleavage of the O–O bond in this system. This is also evident from the calculated reaction energies that are endothermic by at least 20 kcal/mol.

Introduction

Non-heme iron enzymes are important catalysts for many biological reactions. Most of them utilize dioxygen for catalytic oxidations of a large variety of substrates.[1−3] Mononuclear non-heme iron enzymes are involved in hydroperoxidation of substrates (lipoxygenase), hydroxylation of aromatic rings (pterin-dependent enzymes), aliphatic hydroxylation (α-ketoglutarate-dependent enzymes), and aromatic ring oxidation and cleavage (Rieske-type dioxygenases; intra- and extradiol dioxygenases). In many of these cases, high-spin ferrous and ferric alkyl- and hydroperoxo intermediates have been postulated, although experimental evidence for such species is rare.[3] The only well-studied systems are the high-spin Fe(III)−alkylperoxo (enzyme-product) complex of lipoxygenase[4−10] and activated bleomycin, which is a low-spin Fe(III)−OOH complex that is

---

* Authors to whom correspondence should be addressed. E-mail: edward.solomon@stanford.edu (E.I.S.); kiyoshif@chem.tsukuba.ac.jp (K.F.).

[‡] Current address: Institut für Anorganische Chemie, Christian-Albrechts-Universität Kiel, Olshausenstrasse 40, 24098 Kiel, Germany.

[§] University of Tsukuba.

[†] Stanford University.

(1) Holm, R. H.; Kennepohl, P.; Solomon, E. I. *Chem. Rev.* **1996**, *96*, 2239−2314.
(2) Que, L., Jr.; Ho, R. Y. N. *Chem. Rev.* **1996**, *96*, 2607−2624.
(3) Solomon, E. I.; Brunold, T. C.; Davis, M. I.; Kemsley, J. N.; Lee, S.-K.; Lehnert, N.; Neese, F.; Skulan, A. J.; Yang, Y.-S.; Zhou, J. *Chem. Rev.* **2000**, *100*, 235−349.
(4) de Groot, J. J. M. C.; Garssen, G. J.; Veldink, G. A.; Vliegenthart, J. F. G.; Boldingh, J.; Egmond, M. R. *FEBS Lett.* **1975**, *56*, 50−54.
(5) Egmond, M. E.; Fasella, P. M.; Veldink, G. A.; Vliegenthart, J. F. G.; Boldingh, J. *Eur. J. Biochem.* **1977**, *76*, 469−479.
(6) Slappendel, S.; Veldink, G. A.; Vliegenthart, J. F. G.; Aasa, R.; Malmström, B. G. *Biochim. Biophys. Acta* **1983**, *747*, 32−36.
(7) Nelson, M. J.; Cowling, R. A. *J. Am. Chem. Soc.* **1990**, *112*, 2820−2821.

10.1021/ic020496g CCC: $25.00

capable of cleaving DNA.[11−18] For the cofactor-dependent enzymes, it has been shown in several cases that the presence of the cofactor is required for reaction of the active ferrous site with O_2. Correspondingly, the postulated mechanisms of both pterin- and α-ketoglutarate-dependent enzymes include a reaction of the cofactor with dioxygen (free or bound to iron) to form a reactive intermediate that subsequently attacks the protein-bound substrate.[3] However, no such intermediate has yet been identified.

In the case of the pterin-dependent enzymes, the cofactor and the substrate are not directly coordinated to the ferrous active site, but stored in a protein pocket close to the iron center.[19−22] Importantly, the presence of the tetrahydropterin cofactor and substrate causes the ferrous site to become five-coordinate.[19,21] Thus, the site is now activated for reaction with O_2, which can attack either the ferrous iron (pathway B in Scheme 1) or the tetrahydropterin (pathway A).[3,23,26,27] Reaction with the metal would create an $\mathrm{Fe(II)-O_2}$ adduct, which could then attack the pterin ring forming a bridged Fe(II)−OOPtn intermediate as has been proposed on the basis of ^{18}O kinetic isotope data.[28] Alternatively, pathway A leads to the generation of hydroperoxo−pterin (PtnOOH), which could itself be the hydroxylating intermediate[29,30] or which could coordinate to iron(II) forming the same Fe(II)−OOPtn species as in pathway B. This latter intermediate could also be the hydroxylating agent, or it could decay by heterolytic cleavage of the O−O bond forming a reactive $\mathrm{Fe(IV)=O}$ species and the experimentally observed pterin product Ptn−OH. However, these are mechanistic speculations and the exact nature of the hydroxylating intermediate in the pterin-dependent enzymes is not known.

Scheme 1

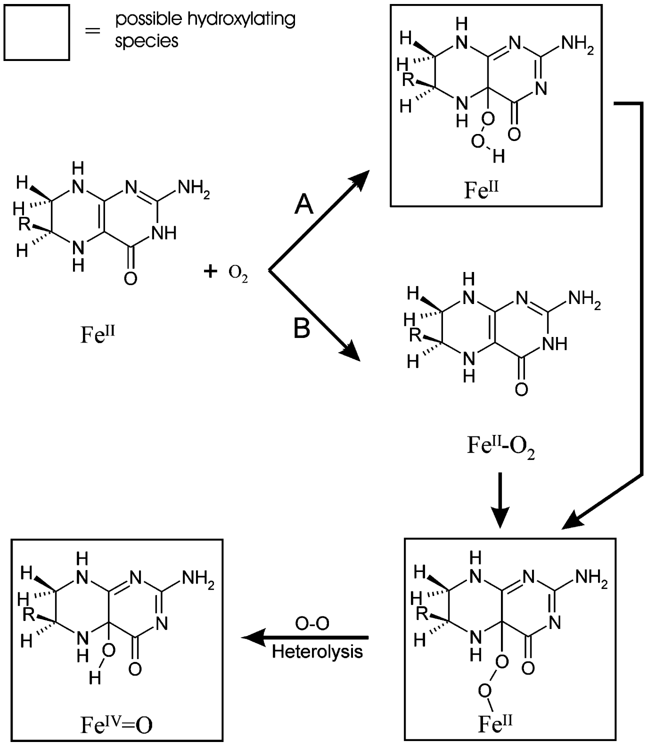

So far, model complexes have primarily been used to explore the electronic structure and reactivity of Fe(III)−alkyl- and hydroperoxo complexes.[3] It has been shown that low-spin Fe(III)−OOR (R = alkyl, H) complexes decay by homolytic cleavage of the O−O bond,[16,31−38] whereas this reaction is orbital forbidden for corresponding high-spin systems.[39] This difference in reactivity is reflected by the electronic structure and vibrational properties of these systems. Low-spin Fe(III)−OOR complexes have strong Fe−O and weak O−O bonds (typical force constants are 3.5 mdyn/Å for Fe−O and 2.9 mdyn/Å for O−O[36]), which is opposite to the values obtained for corresponding high-spin systems.[39] In this study, the spectroscopic properties and the electronic structure of the four-coordinate complex high-spin $[\mathrm{Fe^{III}(L3)(OO^tBu)}]^+$ (**1**; L3 = hydrotris(3-*tert*-

---

(8) Nelson, M. J.; Seitz, S. P.; Cowling, R. A. *Biochemistry* **1990**, *29*, 6897−6903.

(9) Nelson, M. J.; Chase, D. B.; Seitz, S. P. *Biochemistry* **1995**, *34*, 6159−6163.

(10) Skrzypczak-Jankun, E.; Bross, R. A.; Carroll, R. T.; Dunham, W. R.; Funk, J., M. O. *J. Am. Chem. Soc.* **2001**, *123*, 10814−10820.

(11) Burger, R. M.; Peisach, J.; Horwitz, S. B. *J. Biol. Chem.* **1981**, *256*, 11636−11644.

(12) Burger, R. M.; Kent, T. A.; Horwitz, S. B.; Münck, E.; Peisach, J. *J. Biol. Chem.* **1983**, *258*, 1559−1564.

(13) Sam, J. W.; Tang, X.-J.; Peisach, J. *J. Am. Chem. Soc.* **1994**, *116*, 5250−5256.

(14) Westre, T. E.; Loeb, K. E.; Zaleski, J. M.; Hedman, B.; Hodgson, K. O.; Solomon, E. I. *J. Am. Chem. Soc.* **1995**, *117*, 1309−1313.

(15) Guajardo, R. J.; Hudson, S. E.; Brown, S. J.; Mascharak, P. K. *J. Am. Chem. Soc.* **1993**, *115*, 7971−7977.

(16) Nguyen, C.; Guajardo, R. J.; Mascharak, P. K. *Inorg. Chem.* **1996**, *35*, 6273−6281.

(17) Burger, R. M. *Struct. Bonding* **2000**, *97*, 287−303.

(18) Neese, F.; Zaleski, J. M.; Loeb-Zaleski, K.; Solomon, E. I. *J. Am. Chem. Soc.* **2000**, *122*, 11703.

(19) Loeb, K. E.; Westre, T. E.; Kappock, T. J.; Mitic, N.; Glasfeld, E.; Caradonna, J. P.; Hedman, B.; Hodgson, K. O.; Solomon, E. I. *J. Am. Chem. Soc.* **1997**, *119*, 1901−1915.

(20) Goodwill, K. E.; Sabatier, C.; Stevens, R. C. *Biochemistry* **1998**, *37*, 13437−13445.

(21) Kemsley, J. N.; Mitic, N.; Loeb Zaleski, K.; Caradonna, J. P.; Solomon, E. I. *J. Am. Chem. Soc.* **1999**, *121*, 1528−1536.

(22) Erlandsen, H.; Bjørgo, E.; Flatmark, T.; Stevens, R. C. *Biochemistry* **2000**, *39*, 2208−2217.

(23) Note that tetrahydropterin itself reacts with O_2 in solution in a radical chain reaction.[24−26]

(24) Blair, J. A.; Pearson, A. J. *J. Chem. Soc., Perkin Trans. 2* **1974**, 80−88.

(25) Massey, V. *J. Biol. Chem.* **1994**, *269*, 22459−22462.

(26) Kappock, J. T.; Caradonna, J. P. *Chem. Rev.* **1996**, *96*, 2659−2756.

(27) Fitzpatrick, P. F. *Annu. Rev. Biochem.* **1999**, *68*, 355−381.

(28) Francisco, W. A.; Tian, G.; Fitzpatrick, P. F.; Klinman, J. P. *J. Am. Chem. Soc.* **1998**, *120*, 4057−4062.

(29) Dix, T. A.; Benkovic, S. J. *Acc. Chem. Res.* **1988**, *21*, 101−107.

(30) Moran, G. R.; Derecskei-Kovacs, A.; Hillas, P. J.; Fitzpatrick, P. F. *J. Am. Chem. Soc.* **2000**, *122*, 4535−4541.

(31) Arends, I. W. C. E.; Ingold, K. U.; Wayner, D. D. M. *J. Am. Chem. Soc.* **1995**, *117*, 4710−4711.

(32) Kim, J.; Harrison, R. G.; Kim, C.; Que, L., Jr. *J. Am. Chem. Soc.* **1996**, *118*, 4373−4379.

(33) MacFaul, P. A.; Ingold, K. U.; Wayner, D. D. M.; Que, L., Jr. *J. Am. Chem. Soc.* **1997**, *119*, 10594−10598.

(34) MacFaul, P. A.; Arends, I. W. C. E.; Ingold, K. U.; Wayner, D. D. M. *J. Chem. Soc., Perkin Trans. 2* **1997**, 135−145.

(35) Roelfes, G.; Lubben, M.; Hage, R.; Que, L., Jr.; Feringa, B. L. *Chem. Eur. J.* **2000**, *6*, 2152−2159.

(36) Lehnert, N.; Ho, R. Y. N.; Que, L., Jr.; Solomon, E. I. *J. Am. Chem. Soc.* **2001**, *123*, 8271−8290.

(37) Miyake, H.; Chen, K.; Lange, S. J.; Que, L., Jr. *Inorg. Chem.* **2001**, *40*, 3534−3538.

(38) Lehnert, N.; Neese, F.; Ho, R. Y. N.; Que, L., Jr.; Solomon, E. I. *J. Am. Chem. Soc.*, accepted for publication.

(39) Lehnert, N.; Ho, R. Y. N.; Que, L., Jr.; Solomon, E. I. *J. Am. Chem. Soc.* **2001**, 12802−12816.

butyl-5-isopropyl-1-pyrazolyl)borate;[40,41] ^{t}Bu = *tert*-butyl) are investigated in direct comparison to those of the six-coordinate complex high-spin [Fe(6-Me$_3$TPA)(OH$_x$)-(OO^{t}Bu)]$^{x+}$ (TPA = tris(2-pyridylmethyl)amine, x = 1 or 2)[39] using UV−vis absorption, resonance Raman, EPR, and MCD spectroscopies combined with density functional (DFT) calculations. The observed differences in the spectroscopic properties are correlated with the different coordination numbers of these complexes. DFT calculations are then applied to explore the electronic structure of Fe(III)−OOPtn systems by substitution of the *tert*-butyl residue in [Fe^{III}-(L3)(OOtBu)]$^+$ by the electron rich pterin group, which profoundly effects the electronic structure of the system. Finally, the corresponding reduced Fe(II)−OOPtn system is studied by DFT calculations and the reactivity with respect to O−O heterolysis of this putative intermediate of the pterin-dependent enzymes (cf. Scheme 1) is explored.

Complex **1** has already been studied by UV−vis absorption, EPR, and Raman spectroscopy, but the obtained data are incomplete and no spectral assignments have been presented.[42] In addition, no insight about the electronic structure of this complex is given.

Experimental and Computational Procedures

The Fe(III)−alkylperoxo complex **1** was prepared by adding 3 equiv of *tert*-butylhydroperoxide (^{t}BuOOH; 80% in water) to a solution of the ferrous precursor [Fe(L3)(OH)][40,41] in diethyl ether at −80 °C (dry ice/MeOH). After 1 h at −80 °C, the solution has turned red purple and the reaction is complete. Labeled compounds for Raman spectroscopy were synthesized by the same procedure but using ^{t}Bu^{18}O^{18}OH (50% in 25% of diethyl ether and 25% of *tert*-BuOH; determined by NMR spectroscopy) and d_9-^{t}BuOOH (15% in diethyl ether, determined by idometric titration). The labeled alkylperoxides were synthesized using ^{t}BuMgCl and d_9-^{t}BuMgCl, respectively.[43] For the MCD experiments, complex **1** was synthesized in a 1:1 mixture of diethyl ether and 2-methyltetrahydrofuran, which forms a glass when frozen.

UV−Vis Spectroscopy. Absorption spectra have been recorded in diethyl ether solution at −80 °C on an Otsuka Electronics MCPD-2000 system with an optical fiber attachment (300−1100 nm) for low-temperature measurements.

Raman Spectroscopy. Resonance Raman spectra were measured at an excitation wavelength of 676 nm using a krypton ion laser (Coherent 190C-K) at incident powers of about 25 mW and in a ∼135° backscattering geometry. A Spex 1877 CP triple monochromator (equipped with 1200, 1800, and 2400 groove/mm gratings) has been used together with a back-illuminated CCD camera (Princton instruments LN/CCD-1100PB) as a detector. Samples were prepared as diethyl ether solutions, transferred into NMR tubes, and measured at 77 K in a quarz EPR dewar cooled by liquid N$_2$. Sample concentrations were in the range of ∼20 mM.

EPR Spectroscopy. EPR spectra of **1** were recorded at liquid helium temperatures on a Bruker 220-D SRC spectrometer, equipped with an Air Products Helitran liquid He cryostat. Temperatures were measured with a carbon glass resistor mounted in an EPR tube. Samples for EPR spectroscopy contained about 2 mM Fe.

MCD Spectroscopy. MCD spectra have been obtained on frozen glasses of diethyl ether/isopentane solutions at liquid He temperatures (1.8−25 K). A CD spectropolarimeter (Jasco 810) with S1 and S20 photomultiplier tubes has been used where the sample compartment was modified to accommodate an Oxford instruments SM4-7T magnetocryostat. The samples were frozen in metallic sample compartments between two Infrasil quartz disks separated by 3 mm neoprene spacers. Typical sample concentrations were in the range of 1.0 mM.

Data Analysis. Simulation of the VTVH MCD data of **1** was attempted as described in ref 44. The EPR spectrum of **1** was analyzed in terms of the spin Hamiltonian:

$$H = D(S_z^{\,2} - {}^1/_3 S^2) + E(S_x^{\,2} - S_y^{\,2})$$

where the S are spin operators and D and E are the axial and rhombic zero field splitting parameters, respectively.[45a] The EPR spectrum of **1** shows that for this complex $E/D = 0.33$ (rhombic limit). The absolute value of the ZFS parameter D has been estimated from a simple Boltzmann fit[45b] of the temperature-dependent EPR data.

Density Functional Calculations. Spin-unrestricted DFT calculations using Becke's three-parameter hybrid functional with the correlation functional of Lee, Yang, and Parr (B3LYP[46−48]) were performed using the program package Gaussian 98.[49] The structures of the Fe(III)−alkylperoxo model system high-spin [Fe(L)-(OO^{t}Bu)]$^+$ ($\tilde{\mathbf{1}}$), of the Fe(IV)═O product [Fe(L)(O)]$^+$, of hydroperoxo−pterin (PtnOOH), and of the corresponding alcohol anion (PtnO$^-$) were fully optimized using the LanL2DZ basis set. For the Fe(IV)═O species, a total spin of $S = 2$ has been used which is most stable for four-coordinate complexes with N/O ligation. Note that, for corresponding six-coordinate sites, the Fe(IV)═O species has comparable energies for $S = 1$, 2 whereas $S = 0$ is unfavorable (see ref 36). In addition, the ferric model high-spin [Fe(L)(OOPtn)]$^+$ ($\tilde{\mathbf{2}}$) has been partially optimized using LanL2DZ keeping the Fe−O−O−C(Ptn) dihedral angle and the Fe−O−O and C−O−O angles fixed at the values obtained for $\tilde{\mathbf{1}}$. This is necessary in order to prevent the pterinperoxo ligand from going bidentate with the carbonyl oxygen of the pterin as an additional donor which is not appropriate from the crystal structures of pterin-bound enzymes.[20,22] The structure of $\tilde{\mathbf{2}}$ obtained from the partial geometry optimization has a long C−O distance (1.76 Å) of the peroxo group, which reflects a general weakness of this bond in the DFT calculations. This is evident from calculations on tetrahydropterin−O$_2$ adducts,[50] but is also indicated by the increased C−O

---

(40) Hikichi, S.; Ogihara, T.; Fujisawa, K.; Kitajima, N.; Akita, M.; Moro-oka, Y. *Inorg. Chem.* **1997**, *36*, 4539−4547.

(41) Imai, S.; Fujisawa, K.; Kobayashi, T.; Shirasawa, N.; Fujii, H.; Yoshimura, T.; Kitajima, N.; Moro-oka, Y. *Inorg. Chem.* **1998**, *37*, 3066−3070.

(42) Ogihara, T.; Hikichi, S.; Akita, M.; Uchida, T.; Kitagawa, T.; Moro-oka, Y. *Inorg. Chim. Acta* **2000**, *297*, 162−170.

(43) Walling, C.; Buckler, S. A. *J. Am. Chem. Soc.* **1955**, *77*, 6032−6038.

(44) Neese, F.; Solomon, E. I. *Inorg. Chem.* **1999**, *38*, 1847−1865.

(45) (a) Abragam, A. B. *Electron Paramagnetic Resonance of Transition Ions*; Dover Publications: New York, 1986. (b) Browett, W. R.; Fucaloro, A. F.; Morgan, T. V.; Stephens, P. J. *J. Am. Chem. Soc.* **1983**, *105*, 1868−1872.

(46) Becke, A. D. *Phys. Rev. A* **1988**, *38*, 3098.

(47) Becke, A. D. *J. Chem. Phys.* **1993**, *98*, 1372.

(48) Becke, A. D. *J. Chem. Phys.* **1993**, *98*, 5648.

(49) Frisch, M. J.; Trucks, G. W.; Schlegel, H. B.; Gill, P. M. W.; Johnson, B. G.; Robb, M. A.; Cheeseman, J. R.; Keith, T. A.; Petersson, G. A.; Montgomery, J. A.; Raghavachari, K.; Al-Laham, M. A.; Zakrzewski, V. G.; Ortiz, J. V.; Foresman, J. B.; Cioslowski, J.; Stefanov, B. B.; Nanayakkara, A.; Challacombe, M.; Peng, C. Y.; Ayala, P. Y.; Chen, W.; Wong, M. W.; Andres, J. L.; Replogle, E. S.; Gomperts, R.; Martin, R. L.; Fox, D. J.; Binkley, J. S.; Defrees, D. J.; Baker, J.; Stewart, J. P.; Head-Gordon, M.; Gonzalez, C.; Pople, J. A. *Gaussian 94/98*; Gaussian, Inc.: Pittsburgh, 1995.

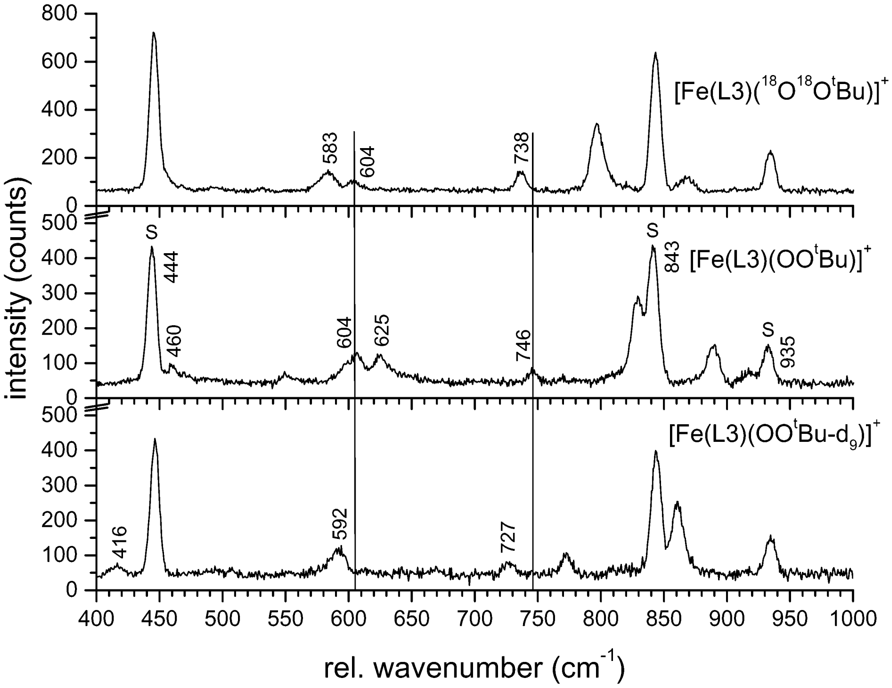

Figure 1. Resonance Raman spectra of **1**. From top to bottom: ^{18}O-substituted ligand; natural abundance isotopes (nai) spectrum; ligand with fully deuterated *tert*-butyl group.

bond length of the peroxo group in PtnOOH compared to ^{t}BuOOH. The corresponding ferrous high-spin [Fe(L)(OOPtn)] ($\tilde{\mathbf{3}}$) complex has been optimized accordingly keeping the Fe−O−O−C unit frozen but allowing *r*(Fe−O) and *r*(O−O) to reoptimize. The LanL2DZ basis set applies Dunning/Huzinaga full double-ζ (D95)[51] basis functions on first row and Los Alamos effective core potentials plus DZ functions on all other atoms.[52,53] Solvation effects were included in the calculations using the polarized continuum model (PCM).[54] Acetonitrile ($\epsilon = 37$) and a continuum with $\epsilon = 10$ were used as the solvent to simulate the protein matrix. In all these calculations, convergence was reached when the relative change in the density matrix between subsequent iterations was less than 1×10^{-8}. Force constants in internal coordinates were extracted from the Gaussian output using the program Redong (QCPE 628).[55]

The MO diagrams of $\tilde{\mathbf{1}}-\tilde{\mathbf{3}}$ were obtained from spin-unrestricted calculations that have been performed with the Amsterdam density functional (ADF) program version 2.0.1[56,57] using the local density approximation (LDA) together with gradient corrections for exchange (Becke88[58]) and correlation (Perdew86[59]). An uncontracted valence triple-ζ Slater-type basis set was used (ADF basis set IV) for all atoms with an additional set of f functions (exponent $\alpha = 1.5$) on iron. Core orbitals through 1s (C, N, O) and 3p (Fe) were frozen in the calculations. Orbitals were plotted with the program Cerius2.

The donor orbitals of the free ^{t}BuOO$^-$ ligand have been described in ref 36. The HOMO of ^{t}BuOO$^-$ is the π^* orbital that is perpendicular to the O−O−C$_{3t}$ plane, labeled π^*_v (v = vertical). The corresponding bonding combination, π^b_v, is located at lower energy. Both of these orbitals are potential π donors to the d functions of iron(III). Next in energy to the HOMO is the in-plane (relative to the O−O−C$_{3t}$ plane) π^* orbital, which is labeled π^*_h (h = horizontal). The corresponding bonding combination π^b_h is located at low energy and strongly mixed with σ^b, which is the bonding combination of the oxygen p functions oriented along the O−O bond. The three orbitals π^*_h, π^b_h, and σ^b are potential σ donors to the d functions of iron. In addition, the ^{t}BuOO$^-$ ligand has one empty acceptor orbital which is labeled σ^*. This is the antibonding combination that corresponds to σ^b, and it is located at high energy.

Results and Analysis

A. Spectroscopy and Electronic Structure of [Fe(L3)(OO^{t}Bu)]$^+$.

A.1. Resonance Raman Spectra and Vibrational Assignment. Figure 1 shows the preresonance Raman spectra of high-spin [Fe(L3)(OO^{t}Bu)]$^+$ (**1**) measured at an excitation wavelength of 676 nm. Excitation into the absorption band around 510 nm leads to fast photo-decomposition, and hence, resonance profiles of **1** could not be obtained. In the natural abundance isotopes (nai) spectrum in the middle panel, six bands are observed at 460, 604, 625, 746, 830, and 889 cm^{-1}. The 625 cm^{-1} mode shifts to 583 cm^{-1} on ^{18}O substitution (top panel) and to 592 cm^{-1} on deuteration (bottom panel). The 830 and 889 cm^{-1} features are found at 797 and 868 cm^{-1} in the ^{18}O-labeled compound, showing a distinct redistribution of the resonance Raman intensity with the mode at lower energy gaining intensity. On deuteration, the opposite effect is observed. In this case, the two peaks are located at 773 and 860 cm^{-1} and the one at higher energy is more intense. The peak at 746 cm^{-1} only shows small shifts of 8 cm^{-1} (^{18}O) and 19 cm^{-1} (deuteration). These data

---

(50) Decker, A.; Lehnert, N.; Solomon, E. I. Manuscript in preparation.
(51) Dunning, T. H., Jr.; Hay, P. J. *Modern Theoretical Chemistry*; Schaefer, H. F., III. Ed.; Plenum: New York, 1976.
(52) Hay, P. J.; Wadt, W. R. *J. Chem. Phys.* **1985**, *82*, 270 and 299.
(53) Wadt, W. R.; Hay, P. J. *J. Chem. Phys.* **1985**, *82*, 284.
(54) Cramer, C. J.; Truhlar, D. G. *Chem. Rev.* **1999**, *99*, 2161−2200.
(55) Allouche, A.; Pourcin, J. *Spectrochim. Acta* **1993**, *49A*, 571.
(56) Baerends, E. J.; Ellis, D. E.; Ros, P. *J. Chem. Phys.* **1973**, *2*, 42.
(57) te Velde, G.; Baerends, E. J. *J. Comput. Phys.* **1992**, *99*, 84.
(58) Becke, A. D. *J. Chem. Phys.* **1986**, *84*, 4524.
(59) Perdew, J. P.; Chevary, J. A.; Vosko, S. H.; Jackson, K. A.; Pederson, M. R.; Singh, D. J.; Fiolhais, C. *Phys. Rev. A* **1992**, *46*, 6671.

Table 1. Experimental Resonance Raman Frequencies (Cf. Figure 1) of $[Fe(L3)(OO^tBu)]^+$ in Diethyl Ether

mode	frequency (cm^{-1})		
	nai	$^{18}O-^{18}O^tBu$	OO^tBu-d_9
$\nu(OO)$	889/830	797	860
$\nu_s(CC)$		868	773
$\nu(CO)$	746	738	727
$\nu(FeO)$	625	583	592
$\delta(OCC/CCC)$	460 (?)	not observed	416

are very similar to the Raman spectra obtained for high-spin $[Fe(6\text{-}Me_3TPA)(OH_x)(OO^tBu)]^{x+}$ and can be assigned as shown in Table 1 on the basis of the analysis presented in ref 39. Accordingly, the peak at 625 cm^{-1} is assigned to the Fe−O stretch. The combined O−C−C/C−C−C bend that has been observed for high-spin $[Fe(6\text{-}Me_3TPA)(OH_x)(OO^tBu)]^{x+}$ at 469 cm^{-1} is most probably identified with the small shoulder at 460 cm^{-1} in the nai spectrum of **1** that shifts to 416 cm^{-1} on deuteration. The peaks at 889 and 830 cm^{-1} correspond to the O−O stretch that is strongly mixed with the symmetric C−C stretch in the nai compound. This situation changes on isotope substitution. In the ^{18}O case, $\nu(OO)$ shifts down to 797 cm^{-1} and, correspondingly, the mixing with $\nu_s(CC)$ at 868 cm^{-1} becomes small. Hence, the latter mode loses most of its intensity. Alternatively, deuteration of the *tert*-butyl group shifts $\nu_s(CC)$ to 773 cm^{-1}, which becomes weak in intensity, whereas $\nu(OO)$ is now located at 860 cm^{-1}. Importantly, these data provide new insight into the mode mixing between $\nu(OO)$ and $\nu_s(CC)$, because all shifted components are visible in the Raman spectra of **1**. This was not the case for high-spin $[Fe(6\text{-}Me_3TPA)(OH_x)(OO^tBu)]^{x+}$, and therefore, these results confirm the vibrational assigment[60] obtained in ref 39. The peak at 746 cm^{-1} is assigned as the C−O stretch.

The calculated force constants for high-spin $[Fe(6\text{-}Me_3TPA)(OH_x)(OO^tBu)]^{x+}$ [39] of 3.62 mdyn/Å for $\nu(OO)$ and 3.05 mdyn/Å $\nu(FeO)$ obtained from NCA are also appropriate for **1**. This is evident from their similar vibrational energies: in both compounds, $\nu(OO)$ is found at 860 cm^{-1} (in the deuterated compound where mode mixing is small) and $\nu(FeO)$ is located at 625 and 637 cm^{-1}, respectively. Therefore, the overall bonding in these compounds must be similar and **1** is also characterized by a strong O−O and a weaker Fe−O bond, which is opposite to the values found in low-spin Fe(III)−OOR systems.[36,38]

A.2. UV−Vis Absorption and MCD. Figure 2, top, shows the absorption spectrum of **1** recorded in diethyl ether solution. A broad absorption band is observed around 19650 cm^{-1} (510 nm; $\epsilon = 700\ M^{-1}\ cm^{-1}$). At higher energy, additional peaks are present at about 30500 and 36000 cm^{-1}. No further distinct absorption band can be identified from the UV−vis spectrum. The low-temperature MCD spectrum of **1** shown in Figure 2, bottom, was used to gain further insight into the different absorption bands. Variable-temperature variable-field (VTVH) MCD data obtained at 17240, 19760, and 21980 cm^{-1} energy positions (indicated with arrows in Figure 2) along the envelope of the broad absorption around 510 nm show an identical nesting behavior. This indicates that this band is due to only one electronic transition and, hence, has to be fitted with one Gaussian. The MCD spectrum also resolves the broad absorption around 30500 cm^{-1} into three bands as shown in Figure 2. This emerges from the fact that the maximum of the MCD spectrum in this energy region is located at 27000 cm^{-1} (370 nm) and, hence, is clearly not aligned with the maximum in the UV−vis spectrum. Using this information, the absorption and MCD spectra of **1** in the $<35000\ cm^{-1}$ region have to be simultaneously fitted with a minimum of four Gaussians as shown in Figure 2. The resulting fit parameters are given in Table 2.

EPR and VTVH MCD. Figure 3, left, gives the EPR spectrum of **1** obtained at 5 K. This complex has an intense signal at $g_{\text{eff}} = 4.3$ and a weak signal at $g_{\text{eff}} = 9.8$ corresponding to a rhombic spin system with $E/D \approx 0.33$. Temperature-dependent EPR data has been obtained, and from a simple Boltzmann fit, a small D value of about 0.3 cm^{-1} has been estimated.

VTVH MCD saturation data obtained for band 1 (at 19760 cm^{-1}) and band 2 (taken at 26320 cm^{-1} to limit the contribution from overlapping band 3; cf. Figure 2) are very similar. Efforts to simulate these VTVH curves using the methodology in ref 44 were unsuccessful due to the small D value and a possible **B**-term contribution precluding saturation at accessible H and T values.

Importantly, the very similar VTVH saturation behavior of bands 1 and 2 indicates that both transitions are polarized along the same molecular axis.[44,61]

From the DFT calculations and in comparison with related Fe(III)−OOR complexes,[36,38,39] band 1 is assigned as an alkylperoxo (π_v^*) to Fe(III) t_2 charge-transfer (CT) transition (vide infra). Hence, the identical VTVH data of bands 1 and 2 indicates that band 2 also has to be identified as an alkylperoxo to Fe(III) CT.

A.3. Donor Strength of the CT States. The results from Raman spectroscopy have shown that the overall Fe−O and O−O bond strengths of **1** and high-spin $[Fe(6\text{-}Me_3TPA)(OH_x)(OO^tBu)]^{x+}$ are similar. In addition, both complexes show an intense transition in the visible region that in both cases is assigned as an alkylperoxo (π_v^*) to Fe(III) $t_{2(g)}$ CT transition (vide infra and cf. ref 39). Hence, it is interesting to compare the relative donor strengths of the different transitions in **1** and the six-coordinate TPA complex. Using the formalism of Baldwin et al.,[62] the donor strength of a ligand is approximately given by

$$(C_{\pi^*}^{M})^2 = (9.22 \times 10^{-2}[\text{Å}])\sum_i \frac{f_i}{\nu_i |\mathbf{r}|^2}$$

with f being the oscillator strength and ν the frequency of

---

[60] Note that the observed shifts on ^{18}O substitution are larger for **1** compared to high-spin $[Fe(6\text{-}Me_3TPA)(OH_x)(OO^tBu)]^{x+}$, because in the latter case only one of the two oxygen atoms of alkylperoxide was isotope labeled.

[61] Lehnert, N.; DeBeer George, S.; Solomon, E. I. *Curr. Opin. Chem. Biol.* **2001**, *5*, 173−184.

[62] Baldwin, M. J.; Root, D. E.; Pate, J. E.; Fujisawa, K.; Kitajima, N.; Solomon, E. I. *J. Am. Chem. Soc.* **1992**, *114*, 10421.

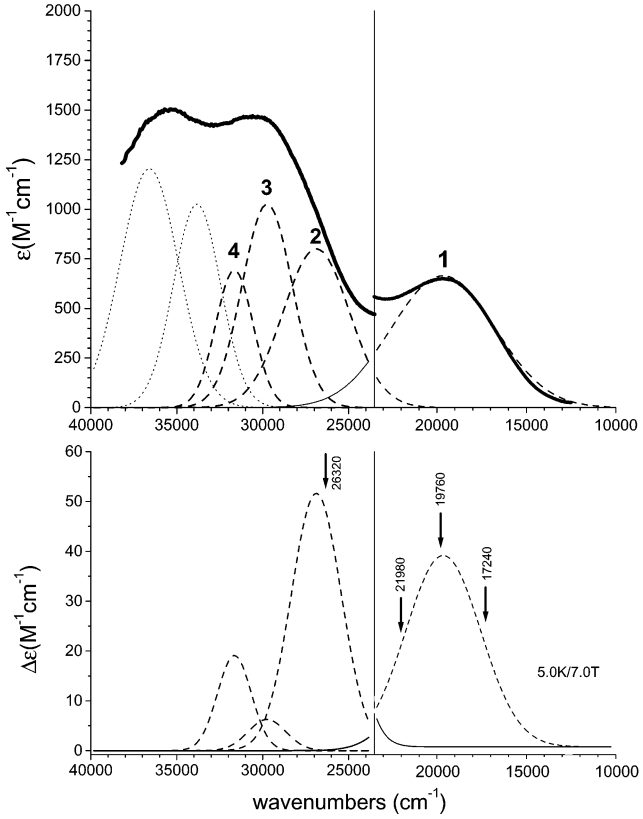

Figure 2. UV–vis (top) and MCD spectra (bottom; recorded at 5 K and 7 T) of **1** together with a simultaneous Gaussian fit (bands 1–4). The low-energy range of the MCD spectrum (bottom, right) is enlarged by a factor of 2. Arrows in the MCD spectrum indicate energies at which VTVH data were recorded (17240, 19760, 21980, 26320 cm^{-1}).

Table 2. Result of the Simultaneous Gaussian Fit of the Absorption and MCD Spectrum

band	ν_{max} (cm^{-1})	ϵ_{max} (M^{-1} cm^{-1})	$\Delta\epsilon_{max}$ (M^{-1} cm^{-1})	f [a]	$\lvert\Delta\epsilon/\epsilon\rvert$
1	19650	665	19.5	0.02074	0.029
2	26880	800	51.7	0.01665	0.065
3	29740	1026	6.3	0.01614	0.006
4	31650	693 (?)	19.1	0.0082	0.03

[a] f: Oscillator strength.

the *i*th CT band; **r** is the transition vector that coincides with the Fe–O bond and can be set to the Fe–O bond length. This equation relates the metal d orbital contributions to the ligand donor orbitals and therefore the strength of the metal–ligand bond to the intensity of the resulting CT transition. The donor strength is calibrated relative to the value obtained for an end-on Cu–peroxide monomer (donor strength set to 1.0). For the π^*_v donor orbital corresponding to band 1 in complex **1**, a low value of 0.21 is obtained compared to 0.5 for high-spin [Fe(6-Me$_3$TPA)(OH$_x$)(OO^{t}Bu)]$^{x+}$ (cf. Table 3). This seems to be inconsistent with the comparable Fe–O bond strengths from Raman spectroscopy for these compounds. However, with the help of VTVH MCD spectroscopy, a second low-energy alkylperoxo to Fe(III) CT is identified for **1** that was not observed for the TPA complex. This second CT transition should have a larger relative donor strength for **1** in order to allow for the similar Fe–O bond strengths in the two compounds. Unfortunately, this transition (a π^*_h to Fe(III) CT; vide infra) could not be observed for the TPA complex (it is located at much higher energy due to the octahedral ligand field; vide infra). This information, however, can be estimated from density functional (DFT) calculations as presented in the next section.

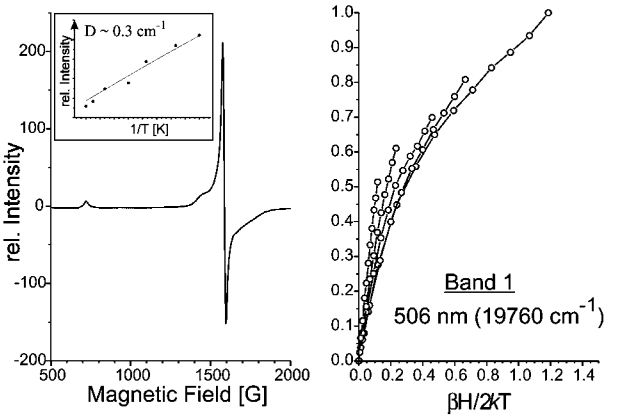

Figure 3. On the left the EPR spectrum of **1** is depicted (recorded at 5 K) together with an inset showing a fit of the intensity of the EPR signal at 1600 G (g_{eff} = 4.3) as a function of temperature. On the right the VTVH MCD data recorded at 506 nm are shown (cf. Figure 2).

A.4. Electronic Structure of [Fe(L3)(OO^{t}Bu)]$^+$. In order to determine the electronic structure of **1**, DFT calculations have been applied on the model [Fe(L)(OO^{t}Bu)]$^+$ ($\tilde{\mathbf{1}}$) where the *tert*-butyl and isopropyl groups on the pyrazol rings of the ligand L3 have been truncated leading to ligand L. Further simplification is not possible, because removal of the closed structure of the tris(pyrazolyl)borate ligand (for example by truncating the borate group that holds the three pyrazol rings together) leads to a very different coordination geometry around iron. Figure 4 shows the fully optimized structure of $\tilde{\mathbf{1}}$ using B3LYP/LanL2DZ. As can be seen, the iron has a trigonally distorted tetrahedral ligand field created by the tris(pyrazolyl)borate ligand. The bond lengths obtained of 1.84 Å for Fe–O and 1.45 Å for O–O given in Table 5 are in good agreement with the crystal structure of [Cu(L1)(OOCm)] (L1 = hydrotris(3,5-diisopropyl-1-pyrazolyl)borate).[63] The calculated frequencies of 618 cm^{-1} for ν(FeO) and 847 cm^{-1} for ν(OO) are in good agreement with experiment (625 and 860 cm^{-1}, respectively). In the following, the optimized structure from B3LYP/LanL2DZ of $\tilde{\mathbf{1}}$ is used for the calculation of the electronic structure of **1** in the coordinate system shown in Figure 4.

The molecular orbital diagram of complex **1** (calculated for $\tilde{\mathbf{1}}$ using the B88P86 functional and a Slater-type triple-ζ (valence) basis set; see Experimental Section) is schematically shown in Scheme 2. In an ideal tetrahedral ligand field, the four ligands are located between the axes of the coordinate system. Correspondingly, the five d functions of the central metal are split into an e set (d$_{x^2-y^2}$, d$_{z^2}$) at lower energy, which undergoes π interactions with ligand orbitals, and a t$_2$ set (d$_{xy}$, d$_{yz}$, d$_{xz}$) at higher energy, which forms σ bonds. However, in the trigonally distorted ligand field of **1** (cf. Figure 4), *the alkylperoxo ligand is located on the x axis*

---

(63) Kitajima, N.; Katayama, T.; Fujisawa, K.; Iwata, Y.; Moro-oka, Y. *J. Am. Chem. Soc.* **1993**, *115*, 7872–7873.

Table 3. Comparison of Relative Donor Strengths and Fe−O Force Constants of Fe(III)−Peroxo Complexes

complex	$\pi^* \rightarrow$ d CT (cm^{-1})	donor strength $(C^{\mathrm{M}}_{\pi^*})^2$ ratio [a]	$\nu_{\mathrm{Fe-O}}$ (cm^{-1})	$k_{\mathrm{Fe-O}}$ (mdyn/Å)	$\nu_{\mathrm{O-O}}$ (cm^{-1})	$k_{\mathrm{O-O}}$ (mdyn/Å)	ref
ls-Fe(TPA)OO^{t}Bu	16000 17364	0.5	696	3.53	796	2.92	36
ls-Fe(N4Py)OOH	17542 19149	0.23	632	3.62	790	3.05	38
hs-Fe(6-Me$_3$TPA)OO^{t}Bu	18123	0.5	637	2.87 (2.10)[c]	860[b]	3.55 (3.69)[c]	39
hs-Fe(L3)OO^{t}Bu	19650 26880	0.21 0.12	625	(2.19)[d]	860[b]	(3.93)[d]	*e*

[a] Corresponds to the charge donation of peroxide to the metal. This value is relative to the donor strength of the $\pi^* \rightarrow$ d CT transition of a Cu−peroxo end-on monomer (set to 1.0).[72] [b] The O−O stretching frequency in the deuterated compound where mode mixing with ν_s(CC) is small. [c] Taken from the DFT calculation on high-spin $[\mathrm{Fe(NH_3)_4(OH)(OO^tBu)}]^+$ where ν(FeO) = 590 cm^{-1} and ν(OO) = 876 cm^{-1}. [d] Taken from the DFT calculation on high-spin $[\mathrm{Fe(L)(OO^tBu)}]^+$ where ν(FeO) = 618 cm^{-1} and ν(OO) = 847 cm^{-1}. [e] This work.

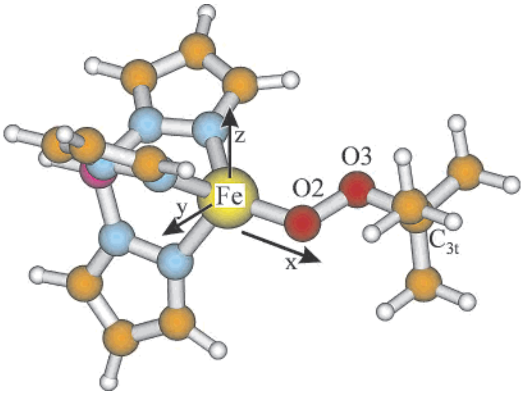

Figure 4. Fully optimized structure (B3LYP/LanL2DZ) of the simplified model $\tilde{\mathbf{1}}$ in which the side chains of the tris(pyrazolyl)borate ligand L3 have been truncated leading to ligand L. The coordinates of $\tilde{\mathbf{1}}$ are given in Supporting Information Table 1. Important structural parameters (bond length in Å, angles in degrees): r(Fe−O) = 1.843; r(O−O) = 1.446; r(C−O) = 1.542; Fe−O−O, 116; C−O−O, 111; Fe−O−O−C, 180.

Table 4. Charge Contributions (in Percent) of Important β Orbitals of $\tilde{\mathbf{1}}$ Calculated with B88P86/Triple-ζ Basis

		energy	Fe	O2		O3		C$_{3t}$	Σpyrazole
no.	label	(hartree)	d	s	p	s	p	s + p	s + p
$\beta\langle 72\rangle$	$\sigma^*\_\mathrm{d}_{xy}$	−0.1413	5	4	33	4	33	2	2
$\beta\langle 68\rangle$	$\mathrm{d}_{xz}\_\pi^*_{\mathrm{v}}$	−0.2507	65	0	15	0	4	0	11
$\beta\langle 67\rangle$	d_{xy}	−0.2624	71	0	1	0	3	0	12
$\beta\langle 66\rangle$	$\mathrm{d}_{\sigma}\_\pi^*_{\mathrm{h}}$	−0.2732	70	0	15	0	1	0	3
$\beta\langle 65\rangle$	$\mathrm{d}_{yz} + \pi^*_{\mathrm{v}}$(nb)	−0.2858	61	0	12	0	10	0	14
$\beta\langle 64\rangle$	d_{nb} (LUMO)	−0.3001	82	0	0	0	1	0	14
$\beta\langle 63\rangle$	$\pi^*_{\mathrm{v}}\_\mathrm{d}_{xz}$ (HOMO)	−0.3284	28	0	14	0	41	0	8
$\beta\langle 56\rangle$	$\pi^*_{\mathrm{h}}\_\mathrm{d}_{\sigma}$	−0.3837	12	0	29	2	23	4	10
$\beta\langle 46\rangle$	$\pi^{\mathrm{b}}_{\mathrm{v}}$	−0.4694	4	0	24	0	17	0	3
$\beta\langle 33\rangle$	$\pi^{\mathrm{b}}_{\mathrm{h}}$	−0.5309	0	0	18	2	21	15	2
$\beta\langle 30\rangle$	σ^{b}	−0.5529	0	0	16	2	17	12	12
$\beta\langle 28\rangle$	σ^{b}	−0.6114	0	3	14	1	22	15	1

and, hence, forms a π bond with a t$_2$ orbital (d$_{xz}$) and a σ bond with an e function (which is therefore labeled d$_\sigma$). The ground state electron configuration of **1** (from EPR) is $[\mathrm{e}]^2[\mathrm{t}_2]^3$ with all five spins aligned giving rise to a high-spin system. In a spin-unrestricted scheme, this corresponds to a situation where all five α-spin d orbitals are occupied whereas the β-spin d orbitals are empty. Hence, only β-spin d orbitals contribute to bonding with donor ligands, and the β-spin MOs will exclusively be analyzed below.

The π^*_{v} orbital of the ^{t}BuOO$^-$ ligand forms a π bond with the β-d$_{xz}$ orbital of iron(III). The corresponding bonding combination, $\pi^*_{\mathrm{v}}\_\mathrm{d}_{xz}$ ($\beta\langle 63\rangle$, cf. Figure 5),[64] is the HOMO of complex $\tilde{\mathbf{1}}$. As given in Table 4, this orbital has about 28% metal contribution, which corresponds to a very covalent interaction. The antibonding combination, $\mathrm{d}_{xz}\_\pi^*_{\mathrm{v}}$ ($\beta\langle 68\rangle$), is found at very high energy, which is due to the fact that d$_{xz}$ is of t$_2$ type and thus shows a σ antibonding interaction with two of the pyrazolyl nitrogen donors (see contour plot in Figure 5). The energy of the corresponding CT transition from $\pi^*_{\mathrm{v}}\_\mathrm{d}_{xz}$ to $\mathrm{d}_{xz}\_\pi^*_{\mathrm{v}}$ can be estimated from the orbital energy differences of these MOs. The value obtained of 17035 cm^{-1} is in accordance with the experimentally determined energy of band 1 in Figure 2 (19650 cm^{-1}; cf Table 2). Therefore, band 1 can be assigned as the $\pi^*_{\mathrm{v}}\_\mathrm{d}_{xz}$ to $\mathrm{d}_{xz}\_\pi^*_{\mathrm{v}}$ CT.[65] The other important interaction between iron(III) and alkylperoxide in $\tilde{\mathbf{1}}$ is mediated by the π^*_{h} orbital, which forms a σ bond with one of the e-type d functions. The corresponding bonding combination, $\pi^*_{\mathrm{h}}\_\mathrm{d}_{\sigma}$ ($\beta\langle 56\rangle$), is shown in Figure 5 and has about 12% metal contribution (cf. Table 4), indicating a strong bond. This is also reflected by the antibonding combination, $\mathrm{d}_{\sigma}\_\pi^*_{\mathrm{h}}$ ($\beta\langle 66\rangle$; cf. Figure 5), which has 16% peroxide character. The energy of the corresponding CT transition from $\pi^*_{\mathrm{h}}\_\mathrm{d}_{\sigma}$ to $\mathrm{d}_{\sigma}\_\pi^*_{\mathrm{h}}$ is estimated from the MO energies to be at 24250 cm^{-1}, which matches with the energy of band 2 in Figure 2 at 26880 cm^{-1}. Taking into account the results from VTVH MCD spectroscopy (vide supra), band 2 can therefore be assigned as the $\pi^*_{\mathrm{h}}\_\mathrm{d}_{\sigma}$ to $\mathrm{d}_{\sigma}\_\pi^*_{\mathrm{v}}$ CT. The other σ donor orbitals of the ^{t}BuOO$^-$ ligand, $\pi^{\mathrm{b}}_{\mathrm{h}}$ and σ^{b}, are nonbonding to the metal. The unoccupied orbital σ^* is mixed with the empty β-d$_{xy}$ function of iron and, hence, does not contribute to net bonding.

Scheme 2, left, shows a simplified representation of the bonding scheme of **1** with the two CT transitions indicated

---

(64) Regarding the nomenclature: "$\pi^*_{\mathrm{v}}\_\mathrm{d}_{xz}$" denotes an MO that is a mixture of the orbitals π^*_{v} and d$_{xz}$; the one with the larger contribution to the MO comes first (in this example π^*_{v}). $\beta\langle 63\rangle$ refers to MO no. 63 with β-spin.

(65) Note that the unoccupied d orbital d$_{yz}$ also has an admixture of π^*_{v}, but the resulting MO "$\mathrm{d}_{yz} + \pi^*_{\mathrm{v}}$(nb)" ($\beta\langle 65\rangle$; cf. Table 4) is nonbonding. The orbital energy difference for the transition from $\pi^*_{\mathrm{v}}\_\mathrm{d}_{xz}$ to $\mathrm{d}_{yz} + \pi^*_{\mathrm{v}}$(nb) is 9350 cm^{-1}, indicating a low-energy CT in **1**. However, a corresponding transition is not observed experimentally and this orbital mixing appears to be overestimated by the calculation.

Table 5. Calculated (B3LYP/LanL2DZ) Geometries and Properties of High-Spin $[Fe(L)(OOR)]^+$ Complexes

	geometric parameters (Å)				spin densities		
Molecule	*r*(Fe−O)	*r*(O−O)	*r*(C−O)	*r*(Fe−N)[a]	Fe	O2	O3
^{t}BuOOH		1.516	1.496				
PtnOOH		1.493	1.570				
hs-$[Fe(L)(OO^tBu)]^+$ ($\tilde{\mathbf{1}}$)	1.843	1.446	1.542	2.01	+3.86	+0.49	+0.16
hs-$[Fe(L)(OOPtn)]^{+\,b}$ ($\tilde{\mathbf{2}}$)	1.878	1.404	1.757	2.02	+3.81	+0.52	+0.26
hs-$[Fe(L)(OOPtn)]^b$ ($\tilde{\mathbf{3}}$)	1.857	1.471	1.757	2.11	+3.62	+0.19	+0.03

[a] Average of all Fe−N distances [b] Geometries are only partly optimized; see Experimental Section.

Scheme 2

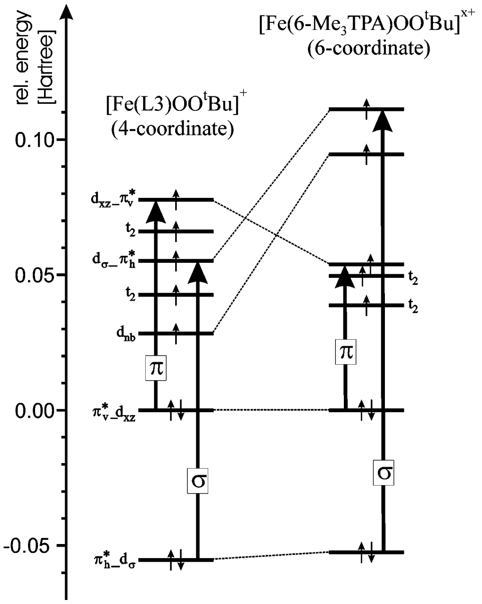

by arrows. Note that the lowest half-occupied orbital of complex **1** (the LUMO in the β-MO scheme; cf. Table 4) is the second e-type d function which is located within the *yz* plane (in the coordinate system in Figure 4) and, hence, is essentially nonbonding and therefore labeled d_{nb}. The overall bonding describtion of complex **1** is very similar to that obtained for the six-coordinate model system high-spin $[Fe(6\text{-}Me_3TPA)(OH_x)(OO^tBu)]^{x+}$ [39] (cf. Scheme 2, right). Differences are mainly due to the different d orbital splittings in the four- and six-coordinate ligand fields of these complexes, respectively. The calculated π^*_v covalency of both compounds is similar, which, however, is in disagreement with experiment. From the relative donor strengths of the corresponding CT transitions (vide supra and cf. Table 3), the covalency should be distinctly higher for the six-coordinate system. Therefore, the π^*_v covalency is overestimated in the calculation of $\tilde{\mathbf{1}}$. The smaller donation in the case of **1** is in agreement with the observed higher energy of the $\pi^*_v\_d_{xz}$ to $d_{xz}\_\pi^*_v$ transition in this complex (19650 vs 18120 cm^{-1} in TPA). This trend in CT energies reflects the higher energy position of the d_{xz} orbital in **1** due to its σ antibonding interaction with two pyrazolyl nitrogen donors. This leads to a larger energy difference between the π^*_v donor and d_{xz} in **1** compared to the six-coordinate TPA complex and, hence, reduced covalency. On the other hand, the σ interaction between π^*_h and d_σ is stronger in **1** as these orbitals are much closer in energy. This is reflected by the lower energy of the $\pi^*_h\_d_\sigma$ to $d_\sigma\_\pi^*_h$ CT in this complex. This is also in agreement with the calculated σ covalency (the π^*_h admixture to d_σ is 16% in **1** vs 9% in the TPA complex) and the experimental observation that the overall bonding is comparable in both compounds (similar Fe−O and O−O vibrational properties), yet the π^*_v donation is lower in **1**. The weaker σ interaction in the six-coordinate complex high-spin $[Fe(6\text{-}Me_3TPA)(OH_x)(OO^tBu)]^{x+}$ is due to the stronger ligand field and greater charge donation compared to **1**, which shifts both $e_{(g)}$-type d orbitals to distinctly higher energies and the corresponding CT out of the spectroscopically accessible range (cf. Scheme 2, right).

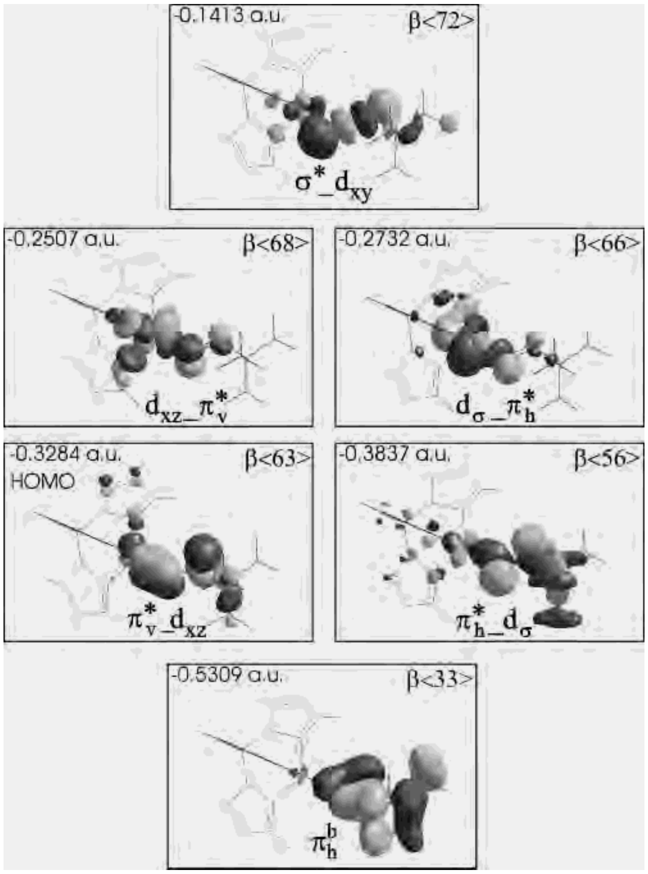

Figure 5. Contour plots of the molecular orbitals of $\tilde{\mathbf{1}}$ (cf. Scheme 2 and Table 4) corresponding to the most important interactions of the alkylperoxo orbitals with the d functions of iron(III) (see text).

B. Electronic Structure of Pterinperoxo Complexes $[Fe(L)(OOPtn)]^{n+}$ ($n = 0, 1$).

B.1. Description of the Electronic Structure of the Free Pterinperoxo Ligand. The fully optimized structure of hydroperoxo−pterin (PtnOOH) is shown in Figure 6 together

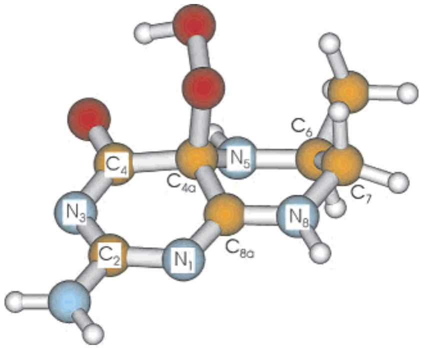

Figure 6. Fully optimized structure (B3LYP/LanL2DZ) of hydroperoxo−pterin (PtnOOH). Important structural parameters (bond lengths in angstroms, angles in degrees): r(O−O) = 1.493; r(C−O) = 1.570; C−O−O, 108; O−O−H, 103; C−O−O−H, 61.

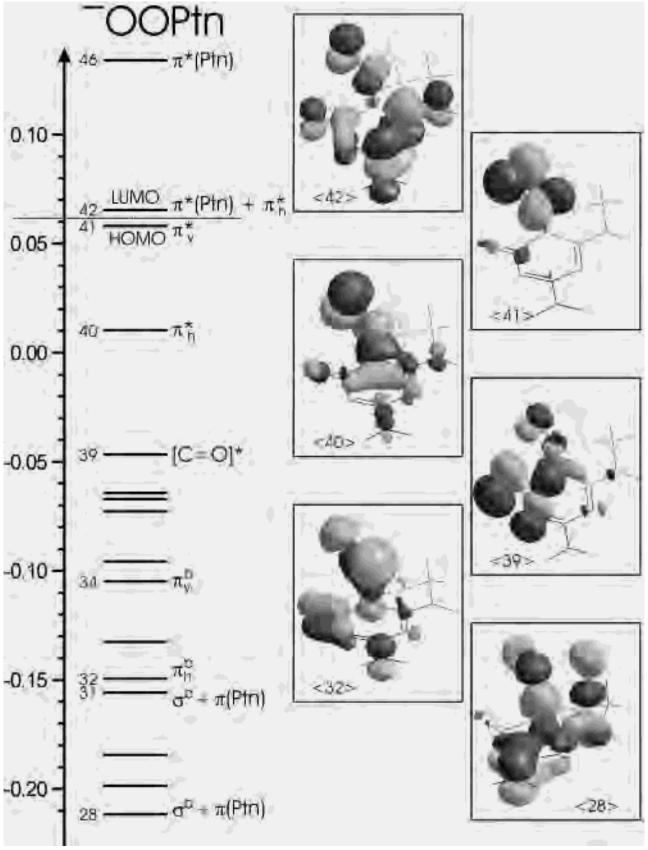

Figure 7. Molecular orbital diagram of the free pterinperoxo ligand (PtnOO^{-}; structure fully optimized with B3LYP/LanL2DZ) calculated with B88P86/triple-ζ basis. Insets show contour plots of important molecular orbitals as indicated.

with the usual numbering of the ring atoms. Geometric parameters are given in Table 5. Importantly, whereas the O−O bond length obtained is comparable to ^{t}BuOOH, the C−O distance of peroxide is distinctly longer for PtnOOH. However, this seems to be related to the DFT calculations and is not an intrinsic feature of the hydroperoxo−pterin molecule (cf. Experimental Section). The MO scheme of the corresponding pterinperoxo ligand of $\tilde{\mathbf{2}}$ (calculated using the B88P86 functional and a Slater-type triple-ζ (valence) basis set) is shown in Figure 7. The HOMO of PtnOO^{-} ($\langle 41\rangle$) is of peroxide π* character and has no contribution from C$_{4a}$ or other ring atoms. In analogy to the HOMO of the free ^{t}BuOO^{-} ligand, this MO is therefore labeled π^*_{v}. Next in energy is the second π* orbital, π^*_{h} ($\langle 40\rangle$), which is bonding toward C$_{4a}$ (cf. Figure 6). These are the most important donor orbitals of the PtnOO^{-} ligand, and they are very similar to the π* orbitals of ^{t}BuOO^{-}. To lower energy, the MO $\langle 39\rangle$ corresponds to an in-plane pterin ring orbital with C=O (carbonyl) antibonding character and is therefore labeled [C=O]*. Importantly, it has some peroxide character as shown in Figure 7. The peroxide π bonding orbitals $\pi^{\mathrm{b}}_{\mathrm{v}}$ and $\pi^{\mathrm{b}}_{\mathrm{h}}$ as well as the σ bonding orbital σ^{b} are located at low energy and do not participate in bonding to high-spin Fe(III) centers as described above for **1**. The LUMO ($\langle 42\rangle$) of the pterin-peroxo ligand is an out-of-plane pterin ring orbital labeled π*(Ptn). As shown in Figure 7, it has a strong admixture of the peroxide π^*_{h} orbital and, hence, could potentially form a back-bond with the metal. Another potentially back-bonding orbital is σ*, which, however, is located at high energy as in the case of ^{t}BuOO^{-}.

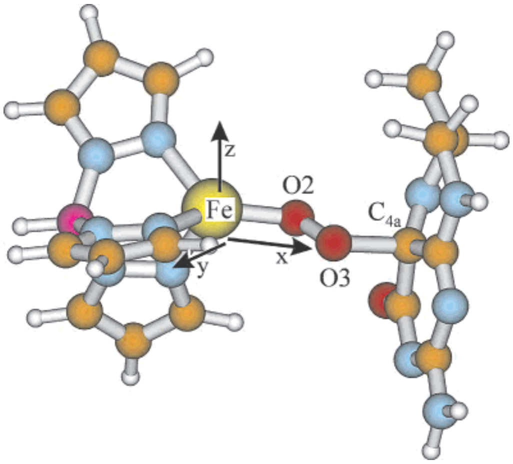

Figure 8. Partially optimized structure (B3LYP/LanL2DZ) of model $\tilde{\mathbf{2}}$ corresponding to an Fe(III)−OOPtn complex. The coordinates of $\tilde{\mathbf{2}}$ are given in Supporting Information Table 2.

B.2. Electronic Structure of [Fe(L)(OOPtn)]$^{+}$. The structure of model system $\tilde{\mathbf{2}}$ (cf. Experimental Section) is shown in Figure 8 together with the appropriate coordinate system, and structural parameters are given in Table 5. The spin density on the peroxide unit is distinctly higher for $\tilde{\mathbf{2}}$ (+0.78) compared to $\tilde{\mathbf{1}}$ (+0.65), which indicates that the covalency between Fe(III) and peroxide is increased in the Fe(III)−OOPtn system. This effect can be evaluated more quantitatively from the MO diagram of complex $\tilde{\mathbf{2}}$ shown in Figure 9 (calculated with the B88P86 functional and a Slater-type triple-ζ (valence) basis set). Due to the high-spin [e]^{2}-[t$_2$]^{3} electron configuration of Fe(III), only β-spin orbitals contribute to bonding with donor ligands (vide supra), and hence, the β-MO diagram of $\tilde{\mathbf{2}}$ is exclusively discussed.

Importantly, the overall bonding scheme of $\tilde{\mathbf{2}}$ is very similar to that obtained for $\tilde{\mathbf{1}}$ (cf. Scheme 2). The pterin-peroxide orbital π^*_{v} interacts with d$_{xz}$ forming a π bond. The corresponding bonding combination, π^*_{v}_d$_{xz}$, is split by interaction with pterin ring orbitals giving rise to MOs $\beta\langle 84\rangle$ and $\beta\langle 83\rangle$ (cf. Figure 9 and Table 6). The antibonding combination, d$_{xz}$_π^*_{v} ($\beta\langle 90\rangle$), is found at high energy due to an antibonding interaction with the pyrazolyl σ donors (cf.

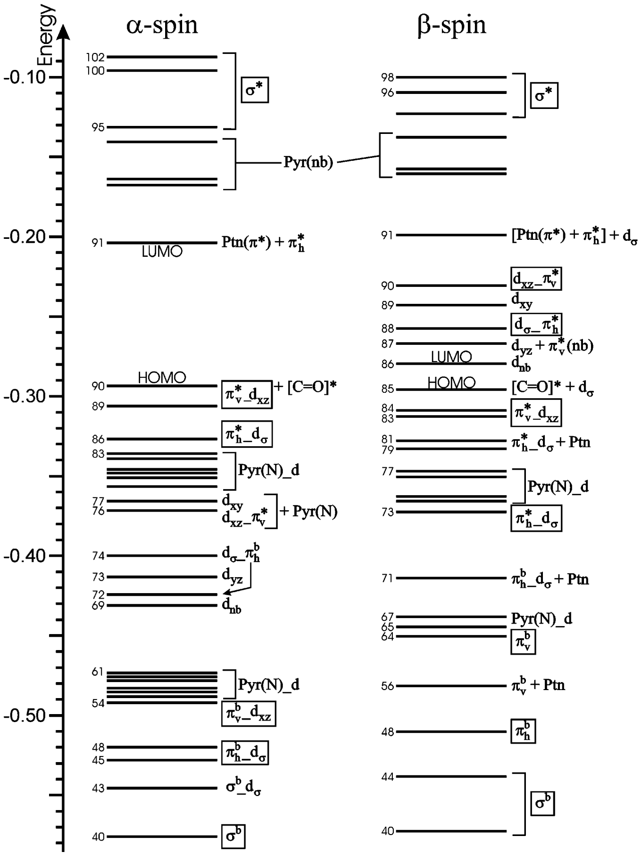

Figure 9. Molecular orbital diagram of $\tilde{\mathbf{2}}$ (in the coordinate system given in Figure 8) calculated with B88P86/triple-ζ basis. The nomenclature "a_b" indicates that orbital a interacts with b and that a has a larger contribution to the resulting MO. Important MOs corresponding to the donor orbitals of the pterinperoxo ligand are marked with a box.

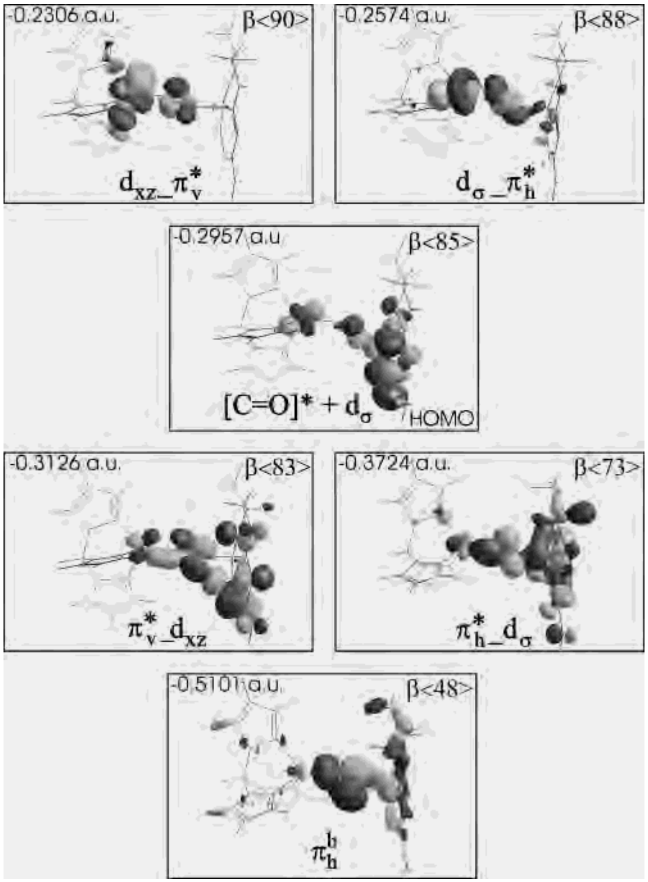

Figure 10. Contour plots of the molecular orbitals of $\tilde{\mathbf{2}}$ (cf. Figure 9 and Table 6) corresponding to the most important interactions of the pterinperoxo donor (π_v^*, π_h^*, [C=O]*, π_h^b) orbitals with the d functions of iron(III).

contour plot in Figure 10) as in the case of $\tilde{\mathbf{1}}$. This orbital has about 15% charge contribution from the peroxide unit (cf. Table 6), which is reduced compared to $\tilde{\mathbf{1}}$ (peroxide admixture: 19%). Hence, the covalency of the Fe–O π bond is somewhat smaller in $\tilde{\mathbf{2}}$. Alternatively, the σ donor orbital π_h^* interacts more strongly with iron(III) in the case of $\tilde{\mathbf{2}}$. Again, the bonding combination, $\pi_h^*\_d_\sigma$, is distributed over several MOs ($\beta\langle 81\rangle$, $\beta\langle 79\rangle$, $\beta\langle 73\rangle$) due to interaction with pterin ring orbitals (cf. Figure 9 and Table 6). The antibonding combination, $d_\sigma\_\pi_h^*$ ($\beta\langle 88\rangle$; cf. Figure 10), has 26% charge contribution from the peroxide unit (cf. Table 6) compared to only 16% in the case of $\tilde{\mathbf{1}}$, which represents a dramatic increase of covalency.

Table 6. Charge Contributions (in Percent) of Important β Orbitals of $\tilde{\mathbf{2}}$ Calculated with B88P86/Triple-ζ Basis

				O2		O3				
no.	label	energy (hartree)	Fe d	s	p	s	p	C4a s + p	Σpyrazole s + p	Σpterin s + p
$\beta\langle 91\rangle$	$[\mathrm{Ptn}(\pi^*) + \pi_h^*] + d_\sigma$	−0.1989	5	0	33	0	9	7	1	68
$\beta\langle 90\rangle$	$d_{xz}\_\pi_v^*$	−0.2307	64	0	11	0	4	1	9	3
$\beta\langle 89\rangle$	d_{xy}	−0.2429	70	1	3	0	3	0	11	2
$\beta\langle 88\rangle$	$d_\sigma\_\pi_h^*$	−0.2574	59	0	19	0	7	1	2	3
$\beta\langle 87\rangle$	$d_{yz} + \pi_v^*(\mathrm{nb})$	−0.2670	64	0	9	0	8	0	12	1
$\beta\langle 86\rangle$	d_{nb} (LUMO)	−0.2798	82	0	0	0	1	0	13	1
$\beta\langle 85\rangle$	$[\mathrm{C{=}O}]^* + d_\sigma$ (HOMO)	−0.2957	16	0	0	0	6	8	1	59
$\beta\langle 84\rangle$	$\pi_v^*\_d_{xz}$	−0.3089	10	0	05	0	12	1	2	64
$\beta\langle 83\rangle$	$\pi_v^*\_d_{xz}$	−0.3126	11	0	8	0	20	1	2	53
$\beta\langle 81\rangle$	$\pi_h^*\_d_\sigma + \mathrm{Ptn}$	−0.3279	4	0	3	0	11	1	3	69
$\beta\langle 79\rangle$	$\pi_h^*\_d_\sigma + \mathrm{Ptn}$	−0.3328	3	0	3	0	8	1	0	74
$\beta\langle 73\rangle$	$\pi_h^*\_d_\sigma$	−0.3724	8	0	23	0	7	8	6	37
$\beta\langle 71\rangle$	$\pi_h^b\_d_\sigma + \mathrm{Ptn}$	−0.4138	1	0	15	0	3	2	0	69
$\beta\langle 64\rangle$	π_v^b	−0.4505	2	0	21	0	17	0	6	43
$\beta\langle 48\rangle$	π_h^b	−0.5101	0	0	24	4	25	4	10	21
$\beta\langle 44\rangle$	σ^b	−0.5384	0	1	13	1	15	9	5	47
$\beta\langle 40\rangle$	σ^b	−0.5726	0	1	7	0	9	8	0	73

Table 7. Charge Contributions (in Percent) of Important β Orbitals of $\tilde{\mathbf{3}}$ Calculated with B88P86/Triple-ζ Basis

		energy	Fe	O2		O3		C4a	Σpyrazole	Σpterin
no.	label	(hartree)	d	s	p	s	p	s + p	s + p	s + p
$\beta\langle 91\rangle$	$d_{xz}\_\pi_v^*$	−0.0606	67	0	7	0	1	0	17	0
$\beta\langle 90\rangle$	d_{xy}	−0.0795	46	0	1	0	7	1	2	30
$\beta\langle 89\rangle$	$d_\sigma\_\pi_h^*$	−0.0875	61	0	10	0	5	0	2	8
$\beta\langle 88\rangle$	$d_{yz} + \pi_v^*$	−0.1041	70	0	11	0	4	0	12	0
$\beta\langle 87\rangle$	$d_\sigma + [\mathrm{Ptn}(\pi^*) + \pi_h^*]$	−0.1056	41	0	2	1	4	4	1	33
$\beta\langle 86\rangle$	d_{nb} (HOMO)	−0.1283	87	0	0	0	1	0	8	1
$\beta\langle 85\rangle$	$\pi_v^*\_d_{xz}$	−0.1663	16	0	24	0	44	1	1	9
$\beta\langle 84\rangle$	$[C{=}O]^* + \pi_h^*\_d_\sigma$	−0.1916	3	0	7	0	16	6	0	62
$\beta\langle 82\rangle$	$\pi_h^*\_d_\sigma + \mathrm{Ptn}$	−0.2065	2	0	7	0	11	4	0	66
$\beta\langle 75\rangle$	$\pi_h^b/\pi_h^*\_d_\sigma$	−0.2401	5	0	34	0	2	7	11	31
$\beta\langle 71\rangle$	π_v^b	−0.2893	2	0	43	0	34	0	1	15
$\beta\langle 60\rangle$	π_h^b	−0.3533	0	0	10	2	15	4	5	54
$\beta\langle 57\rangle$	σ^b	−0.3670	0	0	8	1	7	0	53	18
$\beta\langle 55\rangle$	σ^b	−0.3702	0	0	8	1	6	1	37	36
$\beta\langle 54\rangle$	π_h^b	−0.3733	0	0	8	1	11	2	10	56
$\beta\langle 45\rangle$	σ^b	−0.4114	0	1	8	0	13	14	0	55

In addition to the peroxide donor orbitals π_v^* and π_h^* which are present in both $^t\mathrm{BuOO}^-$ and PtnOO^-, the pterin-peroxo ligand has two more orbitals of interest for bonding to iron(III) (vide supra). In complex $\tilde{\mathbf{2}}$, the HOMO corresponds to the pterin carbonyl orbital [C=O]* (vide supra) with about 16% admixture of the e-type d-function d_σ (β-$\langle 85\rangle$; cf. contour plot in Figure 10). The fact that [C=O]* is higher in energy than π_v^* and π_h^* in complex $\tilde{\mathbf{2}}$ but not in the free ligand (cf. Figure 7) is due to two effects: (a) the strong interaction of both π^* donor orbitals with d functions of iron leads to a large shift of these orbitals to lower energy; and (b) there is a rehybridization of [C=O]*. In the free ligand, [C=O]* has some admixture of π_h^b, but with a very small coefficient on O3 (for labeling see Figure 8) such that it becomes weakly O−O bonding and weakly C−O antibonding. On complexation to Fe(III), the polarization of the peroxide group is reversed and the coefficient on O3 becomes large whereas that on O2 is almost zero. Hence, [C=O]* is now O−O nonbonding and stronger C−O antibonding (cf. Figure 10) and actually shifts to slightly higher energy. Since the electronic matrix element between [C=O]* and the e-type d orbital is small due to low overlap, the strong mixing of these orbitals is a consequence of the high energy of [C=O]* and, therefore, the low ionization energy of PtnOO^-.[66] This allows a transfer of electron density directly from the pterin ring to Fe(III). Another interesting orbital is the LUMO of the free PtnOO^- ligand, labeled "$\pi^*(\mathrm{Ptn}) + \pi_h^*$" (vide supra), which is low in energy. However, it does not mix with any of the occupied α-d orbitals of iron (cf. Figure 9, left). Hence, as expected, the PtnOO^- ligand has no back-bonding properties.

In summary, in going from the $^t\mathrm{BuOO}^-$ to the PtnOO^- ligand in high-spin Fe(III) systems, the overall π^* covalency increases. Additional electron density is transferred to the metal from the pterin ring, which reflects the low oxidation potential of the pterin system. Despite these differences in bonding, the overall ligand fields in $\tilde{\mathbf{2}}$ and $\tilde{\mathbf{1}}$ are very similar and, hence, the same splitting pattern of the d orbitals results, which is depicted in Scheme 2, left. Correspondingly, the LUMO of $\tilde{\mathbf{2}}$ is still the nonbonding e-type orbital d_{nb} which is located in the *yz* plane.

B.3. Electronic Structure of [Fe(L)(OOPtn)] and Heterolytic Cleavage of the O−O Bond. The optimized structure of the high-spin ferrous Fe−OOPtn complex $\tilde{\mathbf{3}}$ (cf. Experimental Section) is very similar to that of $\tilde{\mathbf{2}}$ shown in Figure 8. Structural parameters are given in Table 5. Importantly, the spin density on the peroxide unit is low in $\tilde{\mathbf{3}}$, indicating that covalency is greatly reduced compared to $\tilde{\mathbf{2}}$. This is consistent with a decrease in the effective nuclear charge (Z_{eff}) on the metal in going from ferric to ferrous iron. The MO diagram of $\tilde{\mathbf{3}}$ has been calculated with the B88P86 functional and a Slater-type triple-ζ (valence) basis set. It is very similar to that obtained for $\tilde{\mathbf{2}}$ and shows the d orbital splitting given in Scheme 2, left. It is included in the Supporting Information Figure 1, and charge contributions are presented in Table 7. The π_v^* covalency is reduced in the case of the ferrous system, as evident from the peroxide contribution to $d_{xz}\_\pi_v^*$ ($\beta\langle 91\rangle$ in Table 7), which decreases from 15% in $\tilde{\mathbf{2}}$ to only 8% in $\tilde{\mathbf{3}}$. In parallel, the peroxide character of $d_\sigma\_\pi_v^*$ ($\beta\langle 89\rangle$ in Table 7) is reduced from 26% in $\tilde{\mathbf{2}}$ to 15% in $\tilde{\mathbf{3}}$. Finally, the transfer of electron density from the pterin ring to iron manifested in the admixture of an e-type d orbital (d_σ) into [C=O]* is no longer present in the case of $\tilde{\mathbf{3}}$. Thus, the PtnOO^- ligand donates much less electron density to the ferrous than the ferric site. Importantly, the extra d electron in the case of $\tilde{\mathbf{3}}$ occupies the nonbonding d_{nb} orbital (β-HOMO of $\tilde{\mathbf{3}}$; shown in Figure 11) which is the β-LUMO of $\tilde{\mathbf{2}}$ (cf. Figure 9 and Scheme 2). *Thus, the additional electron does not contribute to activation of the peroxide unit for heterolytic cleavage of the O−O bond.* For this purpose, it would have to occupy the d_{xy} orbital (located at 0.065 hartree in Scheme 2, left) which is capable of forming a back-bond with σ^*.[39] Therefore, the d orbital splitting in the trigonally distorted tetrahedral geometry of the four-coordinate tris(pyrazolyl)borate complex is unfavorable toward activation of peroxo ligands.

---

[66] From the DFT calculations, PtnOOH has a lower vertical ionization energy than ^{t}BuOOH by about 1.2 eV. This is due to the fact that one-electron oxidation of ^{t}BuOOH leads to removal of one electron from the peroxide unit (forming a superoxide species), whereas in the case of PtnOOH the hole is distributed over the pterin ring.

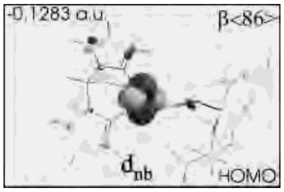

Figure 11. Contour plot of the β-HOMO of $\tilde{\mathbf{3}}$ (cf. Table 7) which corresponds to the doubly occudied d orbital of high-spin Fe(II) (cf. the MO diagram of $\tilde{\mathbf{3}}$ in Supporting Information Figure 1). This orbital is occupied on addition of one electron to the high-spin Fe(III) model system $\tilde{\mathbf{2}}$.

Table 8. Thermodynamics of Heterolytic Cleavage of the O−O Bond in $\tilde{\mathbf{3}}$ (Calculated with B3LYP)

		ΔE (kcal/mol)		
reactant	product[a]	LanL2	+ solv[b] ($\epsilon = 10$)	+ solv (water)
[Fe(L)(OOPtn)] $\tilde{\mathbf{3}}$ ($S = 2$)	$S = 2$	+136	+55	+20

[a] Spin state of the Fe(IV)═O complex; the $^{-}$OPtn anion has $S' = 0$. Total spin: $S_{tot} = 2$. [b] Solv: including a solvent sphere in the calculation using the polarized continuum model (PCM). For the water calculation on $\tilde{\mathbf{3}}$, convergency could not be achieved because of numerical problems. This value is therefore only estimated.

This is also evident from the very unfavorable reaction energies calculated for O−O heterolysis in complex $\tilde{\mathbf{3}}$. As described in the Introduction, a reaction mechanism for the pterin-dependent enzymes has been postulated where an Fe(II)−OOPtn species undergoes heterolytic cleavage of the O−O bond,

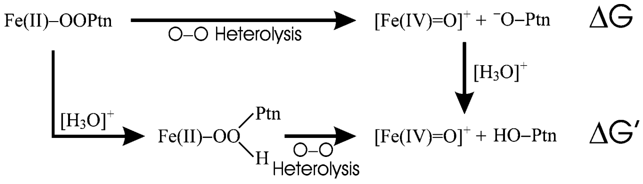

where $\Delta G' = \Delta G - \Delta G^{prot}$ and ΔG^{prot} can be calculated from the pK_A value of PtnOH:

$$\mathrm{PtnOH} + \mathrm{H_2O} \rightarrow \mathrm{PtnO^-} + \mathrm{H_3O^+};\quad \Delta G^{prot} = -RT \ln K_A$$

The free reaction energy ΔG can be estimated from DFT calculations. For this purpose, the structures of the product species Fe(IV)═O ($S = 2$) and PtnO$^-$ have been fully optimized with B3LYP/LanL2DZ (see Experimental Section). Using the LanL2DZ basis set, a reaction energy ΔE of +136 kcal/mol is obtained as shown in Table 8. The large endothermicity is due to the charge separation which is very unfavorable in the gas phase. Including a solvent sphere in the calculations with a dielectric of 10 reduces the reaction energy to about +55 kcal/mol. This seems to be a reasonable estimate for the substrate pocket in pterin-dependent hydroxylases.[20,22] Using water with a dielectric of 78 leads to a value of only +20 kcal/mol (cf. Table 8), which demonstrates how strongly reaction energies can be dependent on solvation when charged species are formed. Due to the fact that the structure of $\tilde{\mathbf{3}}$ is not fully optimized, the zero-point correction to the reaction energy and the entropy cannot be obtained. However, their contribution can be estimated for a cleavage of the O−O bond to about −15 kcal/mol.[36,38] Therefore, the resulting free reaction energy ΔG is about +40 kcal/mol for a dielectric of 10, and, hence, this reaction is thermodynamically not accessible. However, a further energy gain is obtained if the Fe(II)−OOPtn species is initially protonated. Assuming a pK_A of about 10−15 for PtnOH, which corresponds to $\Delta G^{prot} \approx 15-20$ kcal/mol, the free reaction energy $\Delta G'$ obtained is about +20 kcal/mol. Compared to the enzyme species, this number is most likely an overestimate since it can be expected that a six-coordinate high-spin Fe(III) species is present which would be more potent in stabilizing an Fe(IV)═O intermediate compared to a four-coordinate site.[67] In any case, these numbers indicate that initial protonation of the Fe(II)−OOPtn species would be important in enabling the heterolytic cleavage of the O−O bond. Taking this into account, the DFT calculations show that O−O heterolysis to produce an Fe(IV)═O ($S = 2$) and PtnOH (which is the primary product of pterin oxidation observed experimentally) is a thermodynamically accessible reaction pathway for pterin-dependent enzymes.

Discussion

Using resonance Raman, UV−vis absorption, EPR, and MCD spectroscopies correlated to DFT calculations, the four-coordinate complex high-spin $[\mathrm{Fe^{III}(L3)(OO^tBu)}]^+$ (**1**) has been investigated. Vibrational features at 625 and 830/889 cm^{-1} have been assigned as the Fe−O and O−O stretch, respectively (the latter is split due to mixing with the symmetric C−C stretch of the *tert*-butyl group; see ref 39). UV−vis spectroscopy shows a broad absorption band at 510 nm that is assigned to the alkylperoxo (π_v^*) to Fe(III) (d_{xz}) CT. The corresponding Fe−O π bond is found to be highly covalent in the DFT calculations with 28% metal d character mixed into π_v^*. However, from the low intensity and thus donor strength of the 510 nm band, this seems to be an overestimate compared to other Fe(III)−OOR complexes as shown in Table 3. With the help of MCD spectroscopy, an additional electronic absorption is located at 370 nm that is polarized along the Fe−O bond and, hence, is assigned to the alkylperoxo (π_h^*) to Fe(III) (d_σ) CT. This is in agreement with the estimated transition energies from DFT. The corresponding Fe−O σ bond is calculated to be less covalent than the π bond having 12% metal d contribution mixed into π_h^*. From the DFT calculations, no further orbital interactions between the alkylperoxide ligand and Fe(III) d orbitals are of importance for the bonding description of **1**. The lowest singly occupied orbital of **1** is an e-type d function of iron, which is nonbonding to all ligands (labeled d_{nb} in Scheme 2).

This bonding description is very similar to that obtained for the six-coordinate complex high-spin $[\mathrm{Fe(6\text{-}Me_3TPA)(OH_x)(OO^tBu)}]^{x+}$.[39] Differences arise from the different d orbital splittings in the octahedral and trigonally distorted tetrahedral ligand fields of the TPA complex and **1**, respectively, as shown in Scheme 2. In particular, this is

---

(67) For example, the reaction energy for O−O homolysis is about +15 kcal/mol higher for the four-coordinate Fe(III)−OO^{t}Bu system $\tilde{\mathbf{1}}$ compared to that in six-coordinate species,[39] which is due to destabilization of the Fe(IV)═O intermediate formed upon cleavage.

evident from the different CT energies of the π^*_{v} and π^*_{h} to Fe(III) CT in these systems. Importantly, *the two* π^* *donor orbitals of alkylperoxide interact with the same types of d orbitals in both the four- and the six-coordinate complex*; i.e., π^*_{v} forms a π bond with a $t_{2(g)}$ function and π^*_{h} undergoes a σ interaction with an $e_{(g)}$ orbital. However, whereas $t_{2(g)}$ orbitals are also π antibonding to the additional ligands in an octahedral environment, they are σ antibonding to the pyrazolyl donors in the tetrahedral ligand field of **1** and hence, shifted to higher energy in the four-coordinate complex (cf. Scheme 2). Therefore, the π^*_{v} to Fe(III) CT is at higher energy in **1** and the corresponding π bond is less covalent compared to the TPA complex. Alternatively, the $e_{(g)}$ d orbitals of iron are σ antibonding to the additional ligands and high in energy in the octahedral TPA complex, whereas they are π antibonding to the pyrazolyl donors and, hence, at low energy in **1**. Therefore, the π^*_{h} to Fe(III) CT is at much higher energy in the TPA complex and could not be observed spectroscopically.[39] Correspondingly, the Fe−O σ bond mediated by π^*_{h} is more covalent in **1**. The total π^* covalency from both the π^*_{v} and the π^*_{h} orbital is comparable in **1** and high-spin $[\mathrm{Fe(6\text{-}Me_3TPA)(OH}_x\mathrm{)(OO^tBu)}]^{x+}$ reflected by their similar Fe−O and O−O vibrational energies (cf. Table 3).

In order to explore the electronic structure of pterinperoxide complexes, the model system high-spin $[\mathrm{Fe^{III}(L)(OOPtn)}]^+$ ($\tilde{\mathbf{2}}$) has been studied with DFT in direct comparison to high-spin $[\mathrm{Fe^{III}(L)(OO^tBu)}]^+$ ($\tilde{\mathbf{1}}$) described above. The MO description obtained for $\tilde{\mathbf{2}}$ is extremely similar to that calculated for Fe(III)−OO^{t}Bu shown in Scheme 2, left. Importantly, the electron rich pterin group leads to increased charge donation to Fe(III) in the Fe(III)−OOPtn complex. This is evident from the increased σ donation mediated by the π^*_{h} orbital of the pterinperoxo ligand and an additional transfer of electron density directly from the pterin ring to Fe(III). The lowest singly occupied orbital is d_{nb} as in the case of **1**. Reduction of $\tilde{\mathbf{2}}$ by one electron leads to the corresponding ferrous high-spin $[\mathrm{Fe^{II}(L)(OOPtn)}]$ complex ($\tilde{\mathbf{3}}$), which is a model for the potential Fe(II)−OOPtn intermediate in pterin-dependent enzymes (see Scheme 1 and Introduction). Again, the bonding scheme obtained is extremely similar to that calculated for $\tilde{\mathbf{1}}$ (cf. Scheme 2, left) and $\tilde{\mathbf{2}}$. Due to the decreased effective nuclear charge (Z_{eff}) on the metal when going from Fe(III) to Fe(II), the Fe−O covalency is greatly reduced in Fe(II)−OOPtn compared to the ferric complex $\tilde{\mathbf{2}}$. This affects both the π^*_{v} and the π^*_{h} donor orbitals of the pterinperoxo ligand whose covalencies are reduced by about 50% in $\tilde{\mathbf{3}}$. In addition, the direct donation of electron density from the pterin ring to iron as observed in $\tilde{\mathbf{2}}$ no longer occurs. In this sense, the pterinperoxo ligand is less activated by the metal in the ferrous compared to the ferric complex.

Activation of the peroxide ligand in the ferrous compound could still be achieved by the extra electron. However, in the four-coordinate complex $\tilde{\mathbf{3}}$, this electron occupies the nonbonding orbital d_{nb} (which corresponds to the lowest singly occupied orbital in $\tilde{\mathbf{1}}$ and $\tilde{\mathbf{2}}$; cf. Scheme 2, left) and, hence, does not participate in bonding. Correspondingly, the O−O bond is not weakened in $\tilde{\mathbf{3}}$ and calculated free reaction energies for O−O heterolysis (the proposed decay pathway of this intermediate; cf. Scheme 1) of about 20 kcal/mol, which includes protonation of the peroxide prior to cleavage, are unfavorable. However, the potential enzymatic Fe(II)−OOPtn intermediate is most probably six-coordinate, which would assist in peroxide activation. In an octahedral ligand field, the extra electron occupies a β-t_{2g} type orbital which could undergo a π interaction with the σ^* orbital of the pterinperoxo ligand, thus weakening the O−O bond.[68] This pathway has been shown to mediate electron transfer in the homolytic cleavage reaction of the O−O bond in low-spin Fe(III)−alkylperoxo complexes where the β-t_{2g} orbitals are partly occupied.[36,39] In addition, work of Baerends et al. on Fenton type catalysts have shown that, in the proposed six-coordinate Fe(II)−OH−OH primary intermediate, there is a strong π interaction between σ^* of peroxide and a t_{2g} function of iron, prior to homolytic cleavage of the O−O bond.[69,70] Further studies on six-coordinate Fe(II)−OOPtn species that model the active site of pterin-dependent enzymes are in progress which will address the question of how O−O heterolysis may work in these systems.[71]

Acknowledgment. This work was supported by the National Institutes of Health (GM-40392 to E.I.S.). We thank Professor K. Okamoto (University of Tsukuba) for his encouragement to this research. N.L. thanks the Deutscher Akademischer Austauschdienst (DAAD) for a postdoctoral fellowship. K.F. acknowledges financial support from the Japan Society for the Promotion of Science (No. 13555257 and 14350471), KAWASAKI STEEL 21st Century Foundation, and the Asahi Glass Foundation. Ms. Andrea Decker is acknowledged for helpful discussions on the structures and reactivities of different pterin species.

Supporting Information Available: MO diagram and additional contour plots of $\tilde{\mathbf{3}}$ and structural parameters of $\tilde{\mathbf{1}}$ and $\tilde{\mathbf{2}}$.

IC020496G

---

(68) Note that this type of back-bonding interaction between the metal and σ^* of the peroxide could also occur for the α electrons. However, due to the increased exchange interaction, the corresponding α-d orbitals are too low in energy for this interaction to be significant.

(69) Buda, F.; Ensing, B.; Gribnau, M. C. M.; Baerends, E. J. *Chem. Eur. J.* **2001**, *7*, 2775−2783.

(70) Ensing, B.; Buda, F.; Blöchl, P.; Baerends, E. J. *Angew. Chem.* **2001**, *113*, 2977−2979.

(71) Decker, A.; Lehnert, N.; Solomon, E. I. Manuscript in preparation.

(72) Baldwin, M. J.; Ross, P. K.; Pate, J. E.; Tyeklar, Z.; Karlin, K. D.; Solomon, E. I. *J. Am. Chem. Soc.* **1991**, *113*, 8671.